JOURNAL OF AIRCRAFT
Vol. 44, No. 1, January–February 2007

Effect of Porosity Strength on Drag Reduction of a Transonic Projectile

A. Ibrahim* and A. Filippone†
University of Manchester, Manchester, M60 1QD England, United Kingdom

DOI: 10.2514/1.23613

A numerical study was conducted to investigate the effect of porosity strength on the drag reduction of projectiles having the secant-ogival-cylindrical-boat-tail shape. The Navier–Stokes equations for axisymmetric flows were applied. Darcy's law was used to model the interface of the main flow and the flow through the porous surface. The effect of changing the porosity strength upstream and downstream the shock position has been investigated on both cylindrical and boat-tail parts. The simulation method was applied to a projectile with a boat-tail angle $\beta = 7$ deg at zero angle of attack, for Mach numbers ranging from 0.7 to 1.3 and a Reynolds number equal to 4.5×10^6 based on the model length. It has been found that the porous surface is very effective in the case where the pressure drag is dominant, especially on the boat-tail. Moreover, the maximum drag reduction can be obtained by optimizing the porosity distribution for regions upstream and downstream of the shock wave position.

Nomenclature

a	=	height of a porous wall adjacent cell
c_D	=	total drag coefficient
c_{dp}, c_{dsf}	=	pressure and viscous drag coefficients
c_p	=	pressure coefficient
D	=	projectile caliber
$f(x)$	=	porosity distribution function
M_∞	=	freestream Mach number
P_i	=	cavity pressure
P_o	=	pressure above the porous surface
q	=	mass flow rate
S_i, S_o	=	cell facet area
S_m	=	mass source
S_{mi}	=	momentum source in the ith direction
S_{mr}	=	radial momentum source
S_{mx}	=	axial momentum source
U_∞	=	freestream velocity
u	=	axial velocity component
V_i	=	cell volume
v	=	velocity component in the radial direction
v_n	=	normal transpiration velocity
w_i	=	cell width
x	=	x coordinate of the cell center
x_1, x_2	=	limits of the porous area
Y^+	=	wall Y^+ Function
y	=	distance from the wall to the cell center
y_i	=	y coordinates of the cell centroid
β	=	boat-tail angle
ρ_i	=	density inside the cavity
ρ_o	=	density over the porous wall
ρ_∞	=	freestream density
σ	=	porosity function
$\sigma_{\max}$	=	maximum porosity factor

Received 3 March 2006; accepted for publication 4 August 2006.

*Post-Graduate Student, School of Mechanical, Aerospace, Civil Engineering.

†Lecturer, School of Mechanical, Aerospace, Civil Engineering, George Begg Building, P.O. Box 88; a.filippone@manchester.ac.uk. Senior Member AIAA (corresponding author).

I. Introduction

DRAG reduction of artillery projectiles has always been an important issue to ammunition designers to increase the ballistic range. There are different ways to reduce the drag during projectile flight in air. Figure 1 displays the different methods of drag reduction, which can be divided into two main groups: 1) reduction of pressure drag and 2) reduction of base drag.

In the first group, reduction of pressure drag is carried out via the amendments of nose shape, increasing the ogive length, or applying the porosity to the projectile surface. The former two methods are traditional ones whereas the latter method has been investigated recently, and it will be discussed thoroughly in this paper. The second group is still a type of pressure drag reduction, but it is classified as a separate group because base drag contributes a large percentage of the total drag. In this group, base drag can be reduced by boat-tailing the projectile, taking into consideration its reverse effect on the projectile stability. In the second category of this group, base bleed unit or the technique of external burning is applied. These devices do not supply energy to the projectile, but they are used to reserve the kinetic energy of the projectile during its flight. They have the disadvantages of bad accuracy and high dispersion of point of fall due to the variation of their working time.

In the past, decreasing the base drag was an essential requirement as long as it had an appreciable value compared with the pressure and viscous drag components. The simplest way to decrease the base drag is the boat-tailing of the projectile end. However, wave drag increases on the boat-tail part due to the normal shock wave that interacts with the boundary layer on this part of the projectile at transonic speeds. So, increasing the wave drag over the boat-tail part is a main disadvantage of a secant-ogival-cylindrical-boat-tail (SOCBT) projectile especially at high boat-tail angles ($\beta \geq 5$ deg). Therefore, the boat-tail drag may offset the decrease in base drag at transonic speeds. Passive control of the normal shock wave/boundary-layer interaction can be applied to the boat-tail part to decrease the diverse effect of the shock wave on total drag.

The idea of a porous surface in aerodynamics was proposed for the first time in 1979 by Dennis Bushnell and Richard Whitcomb of NASA Langley Research Centre. Further experimental studies on an airfoil have been conducted by Bahi et. al [1] and Nagmatsu et. al [2]. These studies showed that the shock wave could be dispersed by applying proper distribution of porosity on the upper wall of an airfoil. This method was applied on projectiles for the first time by Liang and Fu in 1991 [3]. In their numerical study, the porosity was applied to the boat-tail part only at a Mach number equal to 0.96 and zero angle of attack. Three types of porosity distribution function were examined. A parametric study was conducted showing the effect of maximum porosity factor and size of porous region for each

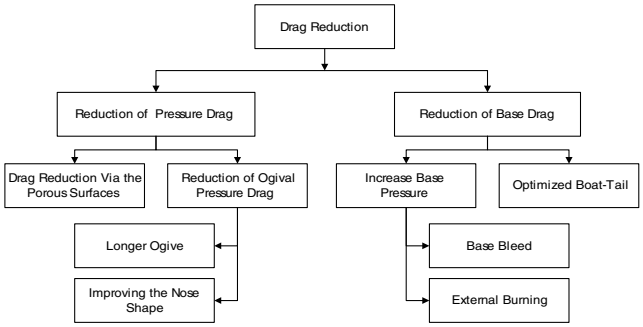

Fig. 1 Illustration of different drag reduction methods.

type of porosity distribution function. Their study showed not only that the porosity decreased the wave drag over the boat-tail but that it also increased the base pressure.

Further numerical studies had been done by Hsiung and Chow. They published two articles concerning the projectile drag reduction using passive control of a normal shock wave/boundary-layer interaction. The first article was published in 1993 [4] in which they had the same approach in their numerical study as that approach of Liang and Fu, but they applied the porosity on both the boat-tail and the cylindrical parts at Mach numbers ranging from 0.9 to 1.2 and angles of attack ranging from 0 to 4 deg. Their computational study showed that total drag reduction of more than 20% can be attained by optimizing the parameters affecting on the porous surface. The second study, which was done by Hsiung and Chow in 1995 [5], presented a new arrangement for the cavity underneath the porous wall by making compartments through splitters. Increases in drag reduction efficiency can be achieved by putting the splitters underneath the porous wall. In 2001 a computational study was done by Onn et. al to investigate the alleviation of Magnus force on the projectile through applying porosity on the boat-tail part of SOCBT projectile [6]. This study showed a remarkable drag reduction by 17.35% of the total drag when applying porosity to the boat-tail part.

All the previous studies applied the porosity of the same strength (maximum porosity factor) to both suction and blowing parts. In our study, the porosity strength on both suction and blowing will be studied individually. This has been carried out by changing the maximum porosity factor over the suction and blowing parts. The maximum porosity factors that have been used are 0.01, 0.03, 0.05, and 0.1 to 0.8 by an increment equal to 0.1.

II. Procedures of Computation

Our numerical study on the SOCBT projectile was carried out by applying a Navier–Stokes equation using the commercial code Fluent. The relative dimensions in terms of projectile caliber are shown in Fig. 2. The two-dimensional Navier–Stokes equations were discretized by using the second-order upwind method for the spatial dependent properties. A coupled implicit scheme was applied to solve the system of differential equations.

The Spalart–Allmaras [7] turbulence model was used in this study. This model was developed for aerodynamic applications and gave

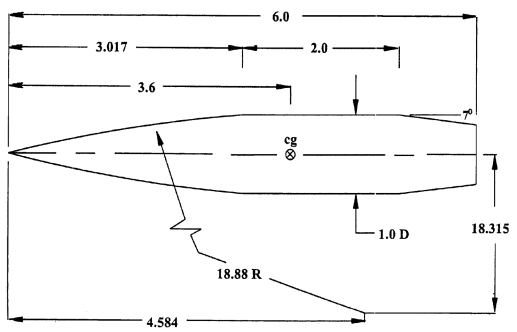

Fig. 2 Relative dimensions of a SOCBT projectile [4].

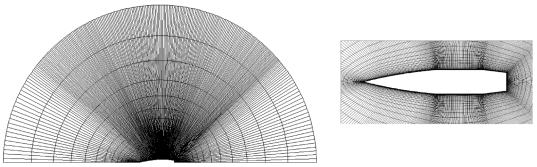

Fig. 3 Construction of an O-grid around the porous projectile.

good results in the present case. It was used with both solid and porous projectiles. The transpiration velocity is used in the interface between the inner and outer flows. This approach is used in highly structured porous surfaces with numerous and sufficiently small pores.

A. Grid Generation

The quality of the mesh plays an important role in getting an accurate and stable solution. A structured quadrilateral O-grid was generated as shown in Fig. 3. To resolve the viscous sublayer, the height of the cell adjacent to the projectile wall has been taken equal to $3.5 \times 10^{-5}D$. Because of the symmetry of the computational domain, it is enough to generate its half, which was divided into five sectors. The division was useful to get smoothness of the grid and proper clustering of the grid near the critical segments of the projectile, where large gradients of the flow are expected. The cells were stretched towards the pressure far field by a ratio equal to 1.25. The grid was 243 nodes in the streamwise direction and 55 nodes in the lateral direction. The pressure far-field boundary was at a distance equal to 23 times the projectile caliber. The value of wall function $Y^+ < 5$ was checked to confirm the sufficient resolution of the mesh near the walls.

B. Boundary Conditions

The pressure far-field boundary was set to the uniform upstream flow. The symmetric boundary was applied to the line coincident with the projectile axis. The no slip condition was set to the solid projectile surfaces. A user-defined function was written to adapt the boundary condition of the porous surfaces. There is no need to simulate the flow inside the cavity, because the change in cavity depth does not affect the drag reduction in any appreciable way and the cavity pressure is nearly constant [8]. To deal efficiently with the porous surface, the porous walls are defined as a cell-face type surface boundary condition as shown in Fig. 4. This boundary condition was implemented by generating a cell zone over the porous wall. Thus the cell zone has a height of one cell adjacent to the porous wall. Sources of mass and momenta will be given to this zone using the calculated transpiration velocity.

Although the flow solver has a definition of the porous medium in case of nonisotropic flow called porous jump, the method used was applied to the porous wall. This remedy of the porous surface boundary condition is more robust and does not need the prediction of permeability that must be fed to the solver in case of using the porous jump boundary condition.

The transpired wall boundary condition was treated by adding a source of mass per unit volume to the continuity equation as the following equation:

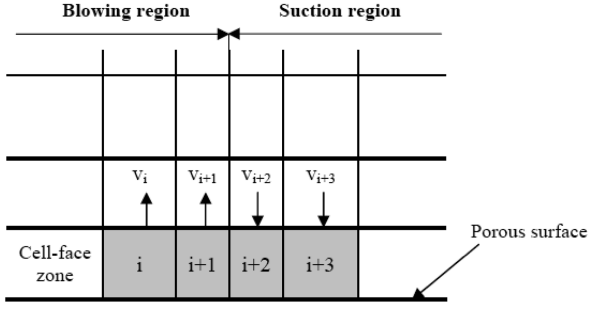

Fig. 4 Transpired wall boundary condition.

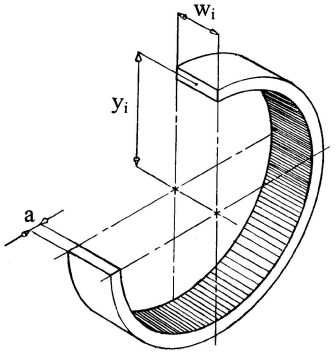

Fig. 5 Cell geometry around the cylindrical part.

$$S_m = \frac{\rho_i v_n S_i}{V_i} \tag{1}$$

The momentum source can be written in the following form:

$$S_{mi} = \oint_s \int (\rho \boldsymbol{v} \cdot \boldsymbol{n}\, \mathrm{d}s) v_i$$

where $\boldsymbol{n}$ is the unit vector normal to the porous surface. The momentum source term is added to the cells of this zone in the radial direction only for porosity over the cylindrical part and in both directions, radial and axial, for porosity over the boat-tail part. Thus, the momentum source for the porous surface on the cylindrical part in the radial direction will be written as

$$S_{\mathrm{mr}} = \frac{\rho_i v|v| S_i}{V_i} \tag{3}$$

where v is equal to v_n. For the boat-tail, there are two components of momentum sources, S_{mx} and S_{mr},

$$S_{\mathrm{mx}} = \frac{\rho_i v_n |u| S_i}{V_i} \sin\beta, \qquad S_{\mathrm{mr}} = \frac{\rho_i v_n |v| S_i}{V_i} \cos\beta \tag{4}$$

where S_i is illustrated as the shaded area in Fig. 5,

$$S_i = 2\pi w_i \left(y_i - \frac{a}{2} \right) \tag{5}$$

The axial and radial velocity components can be determined in terms of the transpiration velocity by the following equations:

$$u = v_n \sin\beta, \qquad v = v_n \cos\beta \tag{6}$$

C. Interface of the Inner and the Main Flows

The simulation of the flow in and out of the porous surface is difficult, because of the large numbers of holes that have a subgrid scale. To overcome this problem, the transpired velocity is used over the whole porous area. This reduces the total number of cells inside the domain and makes a robust numerical solution. By applying Darcy's law, the normal transpiration velocity is calculated from the following equation:

$$v_n = \frac{-\sigma}{\rho_\infty U_\infty} (P_o - P_i) \tag{7}$$

The prediction of the inner pressure inside the cavity enables the determination of the transpiration velocity. Based on several experimental studies, the pressure inside the cavity can be assumed to be constant [8,9]; therefore, P_i will be renamed $\bar{P}_i$. Because q over the porous surface S must be zero,

$$q = \oint_s \int \rho_o v_n \, \mathrm{d}s = 0 \tag{8}$$

By substitution of Eq. (7) into Eq. (8) the inner pressure can be predicted:

$$\overline{P_i} = \frac{\oint_s \int \sigma \rho_o P_o \, \mathrm{d}s}{\oint_s \int \sigma \rho_o \, \mathrm{d}s} = 0 \tag{9}$$

From the known inner mean pressure, the distribution of transpiration velocity over the porous surface can be obtained. A user-defined function is written to adjust the mean pressure inside the cavity using the following equation:

$$\bar{P}_i = \frac{\sum \sigma \rho_o P_o S_o}{\sum \sigma \rho_o S_o} \tag{10}$$

where S_o is the facet area of each cell adjacent to the face-cell zone.

III. Porosity Distribution

The suction/blowing mechanism is controlled to a great extent by the porosity distribution function, which is defined as the ratio between the total area of holes and the area of porous surface. The porosity function can be written as follows:

$$\sigma = \sigma_{\max} f(x) \tag{11}$$

The numerical study investigates the effect of changing of porosity strength applied upstream and downstream of the shock wave position. The porosity function was chosen according to that one used with the Euler study of a porous surface on airfoils by Hartwich [10];

$$\sigma = \sigma_{\max} \sqrt{\sin\left(\frac{x - x_1}{x_2 - x_1} \right) \pi} \tag{12}$$

In transonic speeds, the strongest normal shock waves are nearly formed on the middle of both cylindrical and boat-tail parts at $M_\infty = 0.96$. Thus, our study started to predict the effect of porosity on the drag by applying a porous distribution function with the same $\sigma_{\max}$ upstream and downstream of the shock wave position ($0.01 \le \sigma_{\max} \le 0.8$). So, both suction and blowing regions have the same porosity strength.

Then the effect of the porosity strength over suction and blowing parts can be studied by an individual change of the maximum porosity factor upstream and downstream of the shock wave position. Therefore, the porosity distribution function was changed such that the maximum porosity factor $\sigma_{\max} = 0.01$ to 0.8 was applied to both the suction and blowing regions individually. Figure 6 shows three types of porosity distribution functions. These types have been selected from many combinations of porosity maximum factors applied upstream and downstream of the shock wave. Among all of these combinations, types 1 and 3 gave the extreme values of drag during implementation of our study (see Table 1). Type 2 is presented because it was used before and a comparison could be done with types 1 and 3.

According to the study the was done in [4], maximum lengths of porosity were applied to both cylindrical and boat-tail parts to get the maximum drag reduction. The limits of porosity on the cylindrical part range from $x_1 = 3.12D$ to $x_2 = 4.99D$ and for the boat-tail part range from $x_1 = 5.05D$ to $x_2 = 5.97D$.

IV. Results and Discussions

All the computed results were conducted at a stagnation temperature of 320 K and a Reynolds number of 4.5×10^6, based on the projectile length. The flow past solid and porous projectiles was simulated at $M_\infty = 0.7$, 0.8, 0.9, 0.94, 0.96, 1.1, 1.2, and 1.3 at zero angle of attack.

A. Code Validation

The validation of the code was done through a comparison with experimental data of the pressure coefficient past the solid projectile presented in [4]. Figure 7 shows a comparison between the calculated

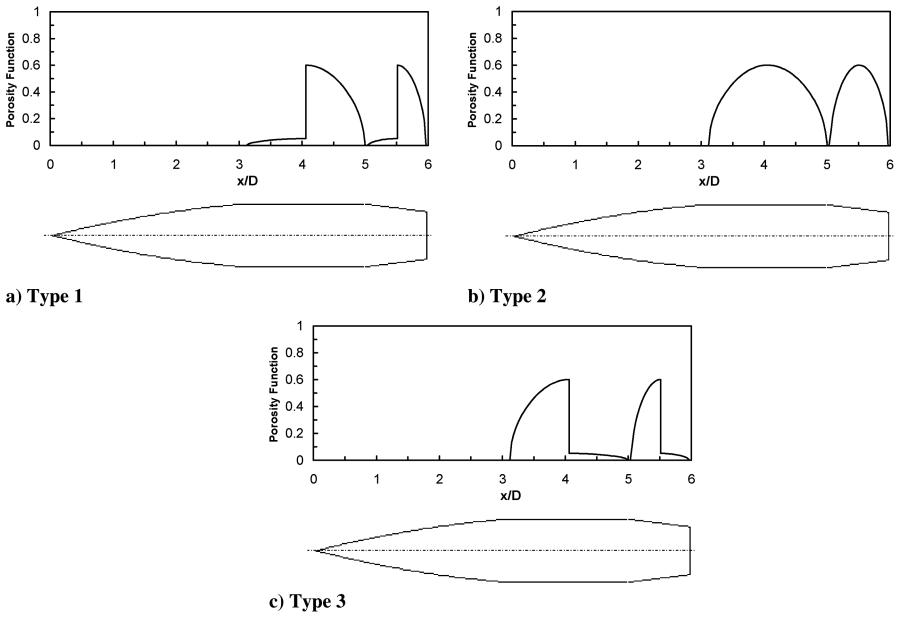

Fig. 6 Porosity distribution functions.

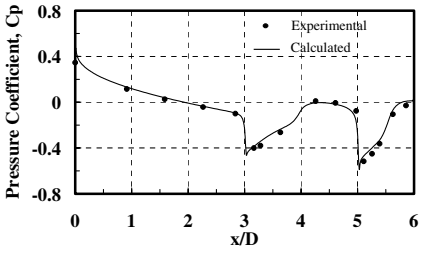

Fig. 7 Pressure coefficient versus normalized length for a solid projectile at $M_\infty = 0.96$.

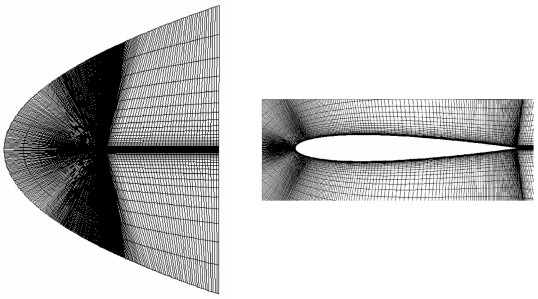

Fig. 8 Construction of a C-grid around the NACA 0012 airfoil.

and measured pressure coefficient for a solid projectile at $M_\infty = 0.96$ and zero angle of attack. There is an excellent agreement with the measured data.

For checking the ability of the code to solve models with porous surfaces, the flow over a full porous cord NACA 0012 airfoil has been simulated at zero angle of attack, $M_\infty = 0.8$, and $Re = 4 \times 10^6$ based on the chord length. A two-dimensional (250×60) grid was generated over the NACA 0012 airfoil as shown in Fig. 8. The grid was constructed such that the porosity is applied to the upper surface (full-chord porosity). The clustering ration is 1.2 towards the walls whereas the height of the cells that are adjacent to the walls was adapted to get Y^+ less than 2.0. The computational domain around the airfoil is approximately ranging from 31 to 47 times the chord length.

The calculated results were compared with experimental ones that were made by Mineck and Hartwich in NASA Langley Research Center [9]. Figure 9 displays a comparison between the calculated and measured pressure coefficient past the upper and lower surfaces for the porous model. For the calculated pressure coefficient over the lower wall, there is a good agreement with the experimental work. However, for the upper wall, there is a discrepancy between the calculated and measured data of the pressure coefficient. According to the study that was done by Bohning and Doerffer [11], this discrepancy could be eliminated by using the three-dimensional approach. But, required powerful computational resources should be taken into consideration. Figure 10 depicts the effect of porosity over the upper wall through the Mach contour lines. The shock wave that should be formed on the upper wall disappears due to the effect of ventilation caused by the porous surface.

B. Drag Force on a Solid Projectile

The drag force was calculated for the solid SOCBT projectile with boat-tail angles $\beta = 5$, 6, and 7 deg. Figure 11 shows the calculated drag coefficients at M_∞ ranges from 0.7 to 1.3 at zero angle of attack. It is noticed that the increase of β is favorable to get lower base drag, but its negative effect on the projectile stability should be taken into consideration [12].

Figure 12 illustrates the percentage of the drag versus the Mach number. This figure shows that the pressure drag is the dominant drag

Table 1 Drag components at each part of both solid and porous projectiles at $M_\infty = 0.96$

	Solid		Type 1		Type 2		Type 3	
	c_{dp}	c_{dsf}	c_{dp}	c_{dsf}	c_{dp}	c_{dsf}	c_{dp}	c_{dsf}
Ogive	0.0313	0.027	0.03158	0.02701	0.03122	0.02702	0.03083	0.02702
Cylinder	0	0.0249	1.75E − 06	0.01926	7.00E − 06	0.03946	2.84E − 05	0.08946
Boat-tail	0.09823	0.00907	0.05885	0.00445	0.06267	0.00998	0.08479	0.03297
Base	0.0226	∼0.0	0.01255	∼0.0	0.00274	∼0.0	0.00816	∼0.0
c_D	0.21312		0.15370		0.17310		0.27326	

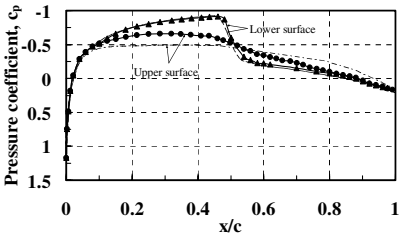

Fig. 9 Pressure coefficient versus normalized length for the NACA 0012 airfoil at $M_\infty = 0.8$.

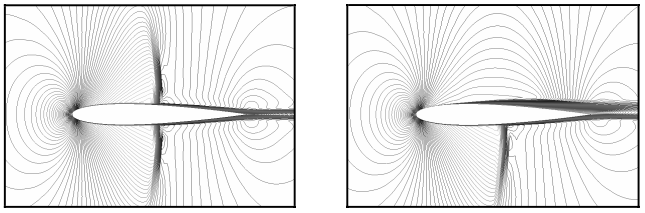

a) Solid surface **b) Full-chord porosity surface**

Fig. 10 Mach contours over both a solid and a porous NACA 0012 airfoil at $M = 0.8$.

force especially at Mach number values starting from 0.9. Therefore, decreasing of the pressure drag via the passive control of the shock wave/boundary-layer interaction will significantly affect the total drag.

C. Effect of Suction/Blowing Mechanism

Generally, the numerical study showed that the suction/blowing mechanism is effective in providing maximum drag reduction, as long as the porosity strength of the region downstream of the shock wave is limited to $\sigma_{\max} = 0.6$ and for the upstream region is limited to $\sigma_{\max} = 0.05$. The effect of the porosity on the boundary-layer profile was determined by taking 30 stations over both cylindrical and boat-tail parts. The boundary-layer edge can be resolved by knowing the axial velocity distribution at each station. Figure 13 displays the boundary-layer profiles past the cylindrical and boat-tail parts of both solid and porous projectiles with types 1 and 3 porosity distributions. The shock wave/boundary-layer interaction can be recognized on the middle of both the cylindrical and boat-tail parts of a solid projectile through the sudden drop in the boundary-layer thickness. But, for a

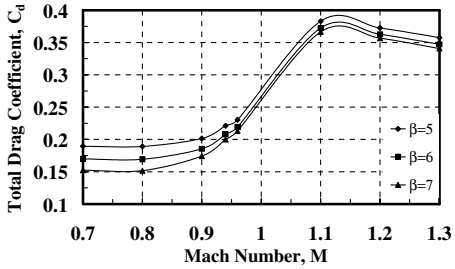

Fig. 11 Total drag coefficient versus M_∞ for a solid projectile.

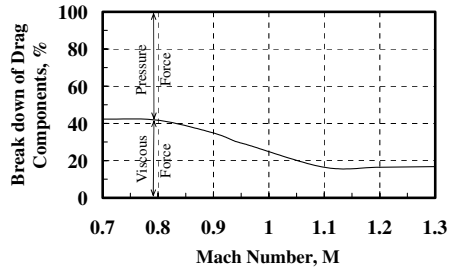

Fig. 12 Breakdown of drag forces acting on the projectile.

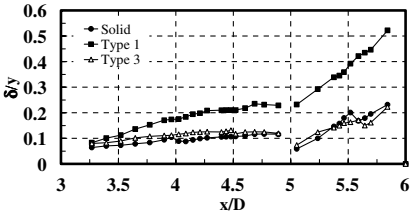

Fig. 13 Boundary-layer profiles over cylindrical and boat-tail parts.

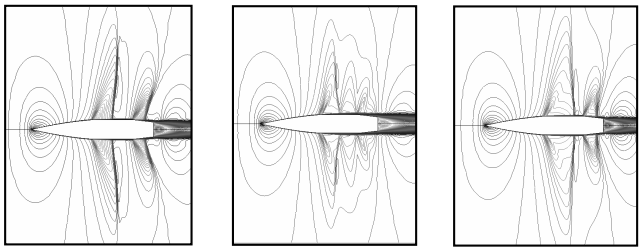

Solid Type 1 Type 3

Fig. 14 Mach contours over both solid and porous projectiles.

porous projectile of type 1, the boundary-layer thickness becomes thicker than those for both solid and type 3 porous projectiles. Although the blowing part of a porous projectile of type 3 has higher porosity than its counterpart in type 1, the boundary-layer thickness in the case of the former one is less than the last. It is thought that the displacement of the shock wave downstream causes a decrease of the suction part resulting in an increase of the transpiration velocity to keep zero mass flux over the porous surface. Because the boundary-layer thickness is controlled by the suction process, it becomes relatively thinner in type 3 due to the strong suction.

Figure 14 shows the Mach contours over the solid and porous projectiles of types 1 and 3. Shock wave positions can be recognized from the clustering of the Mach contours, which gives an indication about the high gradient of flow properties due to the formation of the shock wave. Shock wave displacement in the downstream direction contributes in decreasing the available area for the suction process resulting in a decrease of the inlet mass flow rate resulting in weaker blowing due to the increase of the transpiration area upstream of the shock wave.

On the one hand, blowing is responsible for decreasing the viscous drag, and at the same time it has the disadvantage of increasing pressure drag due to flow separation in case of strong blowing. On the other hand, relatively high porosity strength is favorable in applying to the suction region, which contributes to decreasing the pressure drag by smoothing the pressure distribution over the porous surface. Because the pressure drag on the projectile is dominant, suction is very effective in decreasing the total drag.

Type 1 of the porous distribution function gives the minimum drag reduction. However, type 3 has the adverse effect towards the wave drag. Consequently, type 2 has a moderate effect, because both the regions upstream and downstream of the shock wave have the same porosity strength.

The distribution of c_p for solid and porous projectiles at $M_\infty = 0.96$ is illustrated in Fig. 15. It is shown that the steep pressure rise over the cylindrical part of a solid projectile becomes nearly flat in the case of type 1. The same decrease in the pressure gradient is noticed on the boat-tail part. This gives the opportunity to get a more stable boundary layer. The straightening of the pressure coefficient distribution is due to the pumping of the air upstream.

By changing the distribution function over the porous surface, the suction/blowing mechanism becomes an important process in reducing the wave drag. Figure 16 highlights another explanation for the smoothing of the pressure distribution through displaying the sonic contours. These contours are smoothed and smeared in the streamwise direction for type 1, but the shock wave is strengthened in type 3 and moves in the downstream direction relative to its initial position on the cylindrical part in the case of a solid projectile.

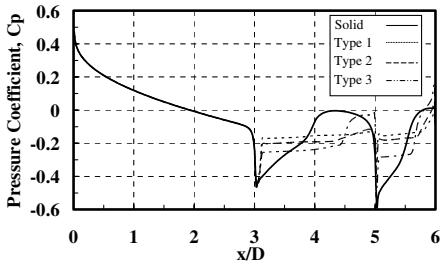

Fig. 15 Pressure coefficient at $M_\infty = 0.96$.

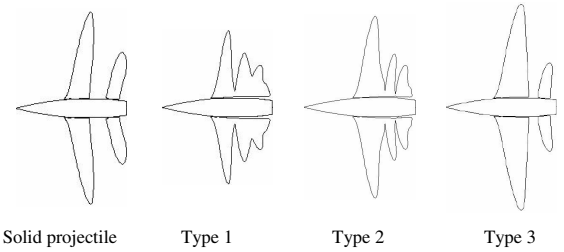

Fig. 16 Sonic Mach contours over solid and porous projectiles.

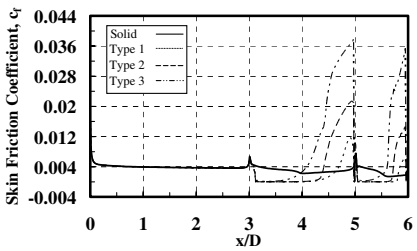

Fig. 17 Comparison of c_f at $M_\infty = 0.96$.

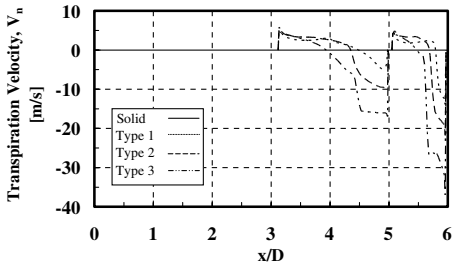

Fig. 18 Comparison of v_n at $M_\infty = 0.96$.

The strength of suction and blowing can be observed by studying the distribution of c_f and v_n in Figs. 17 and 18. Figure 17 shows that the skin friction is increased in the suction part for any porosity type and decreased in the blowing parts. The size of the suction part is small in type 1 and increases gradually in types 2 and 3; consequently, type 1 porosity has the minimum skin friction drag coefficient.

Figure 18 displays the transpiration velocity distributions that provide compatible behavior with the skin friction in size of suction and blowing regions. The transpiration velocity in the suction part is sensitive to the change of the maximum porosity factor compared with its counterpart in the blowing section.

Figure 19 illustrates the change of base pressure due to applying a type 1 porous projectile. The porosity applied to the boat-tail has a negative effect on the base drag, because of the weak recirculation flow behind the base that creates lower pressure than in the case of a solid projectile.

Figure 20 compares the total drag coefficient of a solid projectile and that for a type 1 porous projectile that has the best drag reduction in this study (see Table 1). The percentage of drag reduction versus

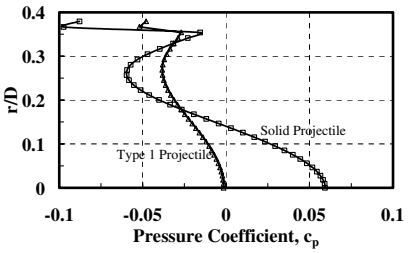

Fig. 19 Coefficient of base pressure at $M_\infty = 0.96$.

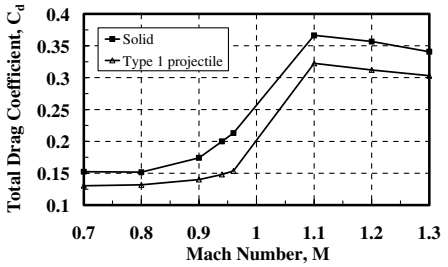

Fig. 20 Total drag coefficient versus Mach number.

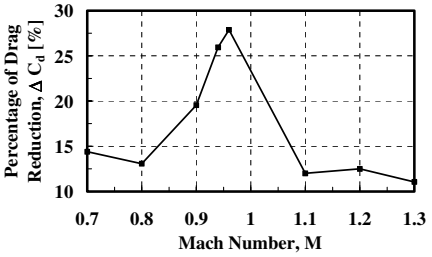

Fig. 21 Percentage of total drag reduction versus Mach number.

the Mach number is shown in Fig. 21. It is noticed that the porosity is very effective in the speed region $0.9 \leq M_\infty \leq 1.2$. A drag reduction of up to 27.5% can be achieved compared with the solid SOCBT projectile.

V. Conclusions

Blowing is responsible for the decrease of the pressure drag, as long as it is not too strong to create flow separation. At the same time, suction is responsible for the control of the boundary layer that is thickened by the blowing process. The normal transpiration velocity in the suction region is sensitive to the changes in the maximum porosity strength rather than the velocity over the blowing region. By using the porosity distribution function, the surface porosity becomes an effective method for decreasing the pressure drag via passive control of the shock wave/boundary-layer interaction. The porous distribution function plays an important role in achieving maximum drag reduction. It is very favorable to decrease the porosity strength of the zone upstream of the shock wave position with a limiting value of $\sigma_{\max} = 0.05$, because lower values do not cause a significant effect on the drag reduction. Simultaneously, increasing the porosity strength of the zone downstream of the shock wave with a limiting value of $\sigma_{\max} = 0.6$ is recommended, because higher values have an adverse effect on the total drag.

References

[1] Bahi, L., Ross, J., and Nagamatsu, H., "Passive Shock Wave/Boundary Layer Control for Transonic Airfoil Drag Reduction," AIAA Paper 83-0137, Jan. 1983.

[2] Nagamatsu, H. T., Dyer, R., and Ficarra, R. V., "Supercritical Airfoil Drag Reduction by Passive Shock/Boundary Layer Control in the Mach Number Range 0.75 to 0.90," AIAA Paper 85-0207, 1985.

[3] Liang, S., and Fu. J., "Passive Control Method for Drag Reduction for Transonic Projectiles," *AIAA 9th Applied Aerodynamics Conference*,

AIAA Paper 91-3213, 1991, pp. 100–108.
[4] Hsiung, J., and Chow, C., "Drag Reduction of Transonic Projectile by Porous Surface," AIAA Paper 93-0417, 1993.
[5] Hsiung, J., and Chow, C., "Computed Drag Reduction on a Projectile Using Porous Surfaces," *Journal of Spacecraft and Rockets*, Vol. 32, No. 3, 1995, pp. 450–455.
[6] Onn, S., Su, A., Wei, C., and Sun, C., "Computational Drag and Magnus Force Reduction for a Transonic Spinning Projectile Using Passive Porosity," *Computer Methods in Applied Mechanics and Engineering*, Vol. 190, Nos. 46–47, 2001, pp. 6125–6139.
[7] Spalart, P. R., and Allmaras, S. R., "A One-Equation Turbulence Model for Aerodynamic Flows," AIAA Paper 92-0439, 1992.
[8] Raghunathan, S., "Passive Control of Shock-Boundary Layer Interaction," *Progress in Aerospace Sciences*, Vol. 25, No. 2, 1988, pp. 271–296.
[9] Mineck, R. E., and Hartwich, P. M., "Effect of Full-Chord Porosity on Aerodynamic Characteristics of the NACA 0012 Airfoil," NASA TP 3591, April 1996.
[10] Hartwich, P. M., "Euler Study on Porous Transonic Airfoils with a View toward Multipoint Design," AIAA Paper 91-3286, 1991.
[11] Bohning, R., and Doerffer, P., "Hybrid and Active Control of the Shock Wave-Turbulent Boundary Layer Interaction and Porous Plate Transpiration Flow," *Euroshock II Project*, Springer–Verlag, Berlin, 2002, pp. 153–177.
[12] Platou, A. S., "Improved Projectile Boat-Tail," *Journal of Spacecraft*, Vol. 12, No. 12, 1975, pp. 727–732.